SAND2015-5723C

Relationship between Acoustic Tones and Flow Structure in Transonic Cavity Flow

Justin L. Wagner,[1] Katya M. Casper,[2] Steven J. Beresh,[3] Srinivasan Arunajatesan,[4] John F. Henfling,[5]
Russell W. Spillers,[6] and Brian O. Pruett[7]
Sandia National Laboratories, Albuquerque, NM, 87185

Particle image velocimetry (PIV) measurements quantified the coherent structure of acoustic tones in a Mach 0.91 cavity flow. Stereoscopic PIV measurements were performed at 10-Hz and two-component, time-resolved data were obtained using a pulse-burst laser. The cavity had a square planform, a length-to-depth ratio of five, and an incoming turbulent boundary layer. Simultaneous fast-response pressure signals were bandpass filtered about each cavity tone frequency. The 10-Hz PIV data were then phase-averaged according to the bandpassed pressures to reveal the flow structure associated with the resonant tones. The first Rossiter mode was associated with large scale oscillations in the shear layer, while the second and third modes contained organized structures consistent with convecting vortical disturbances. The spatial wavelengths of the cavity tones, based on the vertical coherent velocity fields, were less than those predicted by the Rossiter relation. The time-resolved PIV data were bandpass filtered about the cavity tone frequencies to reveal flow structure. The resulting spacing between disturbances was similar to that in the phase-averaged flowfields. Proper orthogonal decomposition (POD) on the stereoscopic data showed modes with qualitatively similar flow structure as the phase-averaged, although the mode numbers were not always consistent with the ranking according to cavity tone energy.

I. Introduction

The flow over an open aircraft bay can result in large levels of aeroacoustic loading associated with broadband turbulence and cavity resonance [1]. The resonant tones amplitudes scale with freestream dynamic pressure [2] and can produce sound pressure levels *SPL* up to about 170 dB [3]. Such pressure fluctuations have motivated numerous cavity studies over the last sixty years, the results of which are reviewed by Rockwell and Naudascher [4], Rowley and Williams [5], and Cattafesta et al. [6].

In subsonic flows, when the cavity length-to-depth ratio L/D is less than about 6-8 [2], the flow category is defined to be 'open' and the interaction of the cavity's acoustic field and free shear layer form a feedback loop that results in cavity resonant oscillations [1]. The resonant modes are primarily longitudinal and in simple rectangular geometries, their frequencies can be reasonably predicted by the semi-empirical relation of Rossiter [1], which was later modified by Heller and Bliss for compressible flows [10]. The mode amplitudes, however, are less predictable as they are complex functions of flow conditions and cavity geometry [5, 6, 7, 11].

An additional complexity lies in the temporal behavior of resonating cavity flows. Although a given cavity flow can be associated with several tonal frequencies, the tones do not necessarily occur simultaneously. Rather the

[1] Senior Member of the Technical Staff, Engineering Sciences Center, P.O. Box 5800, Mailstop 0825; jwagner@sandia.gov. AIAA Senior Member.
[2] Senior Member of the Technical Staff, Engineering Sciences Center, AIAA Senior Member.
[3] Distinguished Member of the Technical Staff, Engineering Sciences Center, AIAA Associate Fellow.
[4] Principal Member of the Technical Staff, Engineering Sciences Center, AIAA Senior Member.
[5] Distinguished Technologist, Engineering Sciences Center, AIAA Member.
[6] Principal Technologist, Engineering Sciences Center.
[7] Senior Technologist, Engineering Sciences Center.

This work is supported by Sandia National Laboratories and the United States Department of Energy. Sandia National Laboratories is a multi-program laboratory managed and operated by Sandia Corporation, a wholly owned subsidiary of Lockheed Martin Corporation, for the U.S. Department of Energy's National Nuclear Security Administration under contract DE-AC04-94AL85000

dominant cavity mode can vary with time – a process known as 'mode-switching'. The idea for mode switching was first proposed in the earlier works of Krishnamurty [12] and Sarohia [13], later proven in the experiments of Kegerise et al. [14, 15], and observed in the simulations of Larcheveque et al. [16] shortly thereafter. In the first demonstration of mode-switching, Kegerise et al. [15] also showed the Rossiter relation to be effective in predicting the number of vortices and vortex spacing in the shear layer for a given mode. Murray and Ukeiley [16] later used particle image velocimetry (PIV), fast-response pressure data, and stochastic estimation to make further observations on the behavior of mode switching. Similar to Kegerise et al. [15], they were able to confirm the proper number of vortices associated with a given Rossiter mode. Moreover, they drew the qualitative conclusion that mode switching was related to an "interference that occurs between the hydrodynamic and acoustic field." Another quite interesting finding was made by Brès and Colonious [18], who suggested that spanwise instabilities can lead to low-frequency modulations of Rossiter modes, a previously unexplained observation reported in the experiments of Kegerise et al. [15].

Although previous studies have provided much insight, many questions remain on the relationship between cavity tones and flow structure. Since cavity flows often contain several competing modes that can switch and/or occur simultaneously in time, it is difficult to discern the effects of a given resonant tone on the flow structure. This is especially true when a cavity flow has several tones of similar amplitude. The current study addresses this challenge by using joint-time frequency analysis to bandpass filter the pressure fluctuations in a transonic resonating cavity flow. Stereoscopic PIV data, acquired simultaneously, are then phase-averaged with respect to the bandpassed pressures to produce the flow structure associated with a given resonant tone. For validation purposes, these results are then briefly compared to those obtained with separate time-resolved PIV data, which were acquired with a burst-mode laser. Finally, a qualitative flowfield interpretation is presented using proper orthogonal decomposition (POD).

II. Experimental Program

A. Trisonic Wind Tunnel (TWT)

Experiments were conducted in the blowdown-to-atmosphere TWT. The facility uses air as the test gas and has a test section enclosed in a pressurized plenum. During a run, the stagnation temperature T_0 was held constant at 321 ± 2K. Data were obtained at freestream Mach numbers M_∞ of 0.60, 0.80, and 0.91, which were measured with a static pressure tap in the wall 200 mm upstream of the cavity. As discussed subsequently, the Mach 0.91 cavity had three active cavity tones making it an ideal case for the current work. Thus, the focus here is at this Mach number. Typical flow conditions for the experiments conducted in the 305 × 305 mm^2 test section are given in Table 1. The freestream dynamic pressure q_∞ was held constant to about 33 kPa. The tunnel wall boundary layers developed naturally and were fully turbulent upon arrival at the test section. Previous measurements have indicated that the 99% wall boundary layer thickness at the cavity entrance ranges is about 13 mm (about half the cavity depth).

Table 1: Typical TWT Experimental Conditions

M_∞	P_0, kPa	Re × 10^{-6}, /m
0.91 ± 0.02	60	13

An acoustic liner with a design similar to that used by other researchers [14, 19-20] was placed in the wall opposite the cavity to mitigate the undesirable acoustical interference associated with solid wind tunnel walls in subsonic cavity flows. As described in a recent study by the current authors, the spanwise walls of subsonic test sections can also lead to acoustical contamination if untreated. To reduce these effects, one spanwise wall of the subsonic test section was replaced with an acoustic dampener, which consisted of a porous wall (used typically for transonic testing) backed by acoustical absorption foam [21]. The opposite spanwise wall was solid with a window providing a view for the PIV cameras.

B. Cavity

The cavity had length L of 127 mm, width W of 127 mm, and depth D of 25.4 mm and was installed in the lower wall of the test section (Fig. 1). With an L/D of 5 the cavity flow category is 'open' and expected to resonate. The streamwise (x), wall-normal (y), spanwise (z) coordinate system originates at the spanwise center of the cavity leading edge. The wind tunnel floor is defined to be at $y = 0$, with positive y pointing away from cavity.

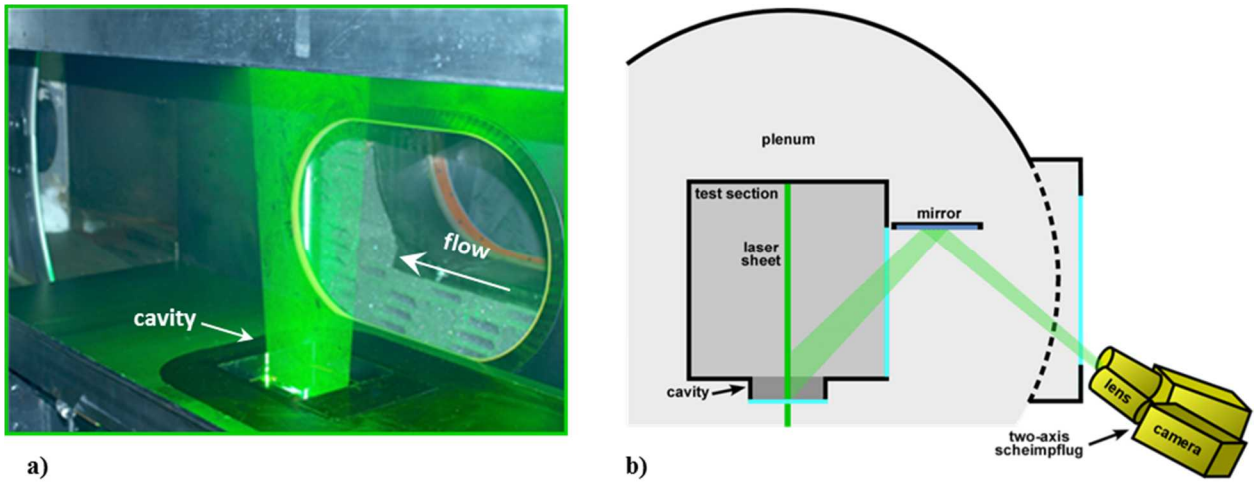

Fig. 1 Cavity and PIV setup: (a) photo showing the cavity in the lower wall of the test section and the PIV laser sheet, (b) illustration of the PIV viewing configuration, which used a mirror to visualize the entire depth of the finite-width cavity (flow direction is into the page).

C. PIV measurements

Two distinct datasets were obtained each with their own advantages. The first used a 10-Hz PIV system to obtain stereoscopic vector fields with high spatial resolution over nearly the entire cavity. The second utilized a pulse-burst PIV system to provide two-component, time-correlated vectors of the cavity resonance phenomena. The time-resolved field-of-view viewed 50% of the cavity depth to capture most of the shear layer.

Seeding was provided by a smoke generator (Corona Vi-Count 5000) that produced a large quantity of mineral oil particles. Particles were delivered to the tunnel stagnation chamber upstream of the flow conditioning section. Measurement of the *in-situ* particle response across a shock wave generated by a wedge has shown the particle size to be about 0.8 µm. Stokes numbers are estimated to be about 0.04 based on *a posteriori* measurements of typical cavity shear layer eddies. Thus, the particles rapidly attain the local velocity even in the presence of velocity gradients in the shear layer [22]. Inspection of the PIV images showed adequate seeding in all portions of the cavity, including the recirculation region.

10-Hz Stereoscopic System

The light source was a frequency-doubled dual-cavity Nd:YAG laser (Spectra Physics PIV-400) that produced about 300 mJ per beam. The beams were formed into coplanar sheets and directed into the test section from beneath the wind tunnel and then entered the cavity through a window forming its floor. The laser sheet thickness was about 1.5 mm, and as is shown in Fig. 1a, it was aligned to the spanwise center of the cavity and filled the entire streamwise length of the cavity.

As detailed in Beresh et al. [23], PIV measurements for rectangular cavities in the TWT have limited optical access due to the presence of the pressurized plenum that surrounds the test section. Moreover, since the cavities are three-dimensional (i.e., they do not span the entire test section width), solid walls obstruct a direct view of a submerged cavity cutout. To overcome this, the cameras were angled to view a mirror in the plenum, which allowed the entire cavity depth to be visualized (Fig. 1b). Particles were imaged with two stereoscopic setups consisting of four cameras (Fig. 2a). The first pair of cameras captured the upstream portion of the cavity ($0.2 < x/D < 2.6$) and the second pair imaged the downstream portion ($2.5 < x/D < 4.8$). This four-camera configuration allowed for nearly the entire cavity to be imaged simultaneously and stereoscopically, without sacrificing spatial resolution.

Each stereoscopic camera setup consisted of two sCMOS cameras (LaVision Imager sCMOS) with a resolution of 2560×2160 pixels^2 digitized at 16 bits. The cameras were fitted with 200-mm focal length lenses and viewed the imaging region using compound angles. Therefore, two-axis scheimpflug [24] focusing was required for this configuration. In each stereo setup, a half-angle of 12-degrees with respect to the spanwise direction was used. Though such a half-angle is sub-optimal for stereoscopic PIV, a greater angle would have occluded the streamwise extent of the field-of-view. Each camera was angled vertically by about 55-degrees to view the plenum mirror (Fig. 1b) and make measurements of the entire cavity depth. An f-number of 11 was found to give an adequate depth-of-field and image intensity.

Stereoscopic camera calibrations were achieved by placing a single-plane alignment target in the position of the laser sheet, then scanning it through the volume of the laser sheet to acquire data at seven spanwise planes. The LaVision PIV software package DaVis v8.2 was used to find a polynomial fit for the calibration. The self-calibration routine in the software was also employed to reduce errors associated with misalignment between calibration target and the true location of the laser sheet.

About 3000 image pairs were acquired at each Mach number. Image pairs were interrogated with an initial pass using 64 × 64 pixel interrogation windows, followed by two iterations of 32 × 32 pixel interrogation windows, incorporating adaptive window offsets and image deformation based upon local velocity gradients. A 50% overlap in the interrogation windows was used. The resulting vector fields were validated based upon signal-to-noise ratio, nearest-neighbor comparisons, and allowable velocity range. About 95% of all vectors obtained were valid. This very same dataset was recently used to quantify the effects of cavity width on the mean flow and turbulence statistics [25]. In contrast, the present goal is to use the data to quantify the flow structure associated with each cavity tone through comparison to band-passed pressure signals. To better reveal coherent flow structures, the vector fields were smoothed with a low-pass filter.

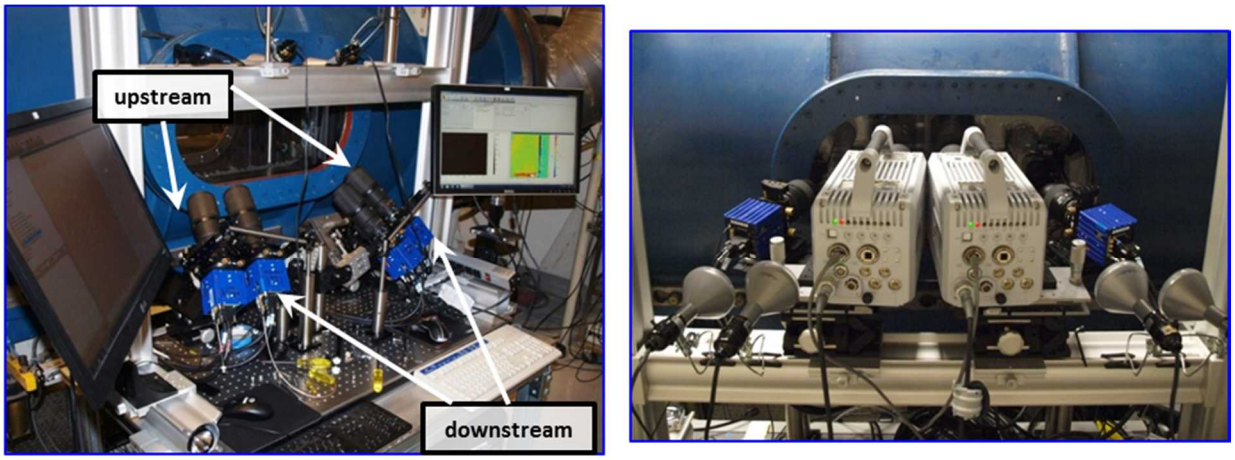

Fig. 2 PIV cameras: (a) stereo configurations of the10-Hz system, and (b) high-speed cameras used in the time-resolved system [Steve: please send me a picture of the new high-speed camera setup].

Time-Resolved (Pule-Burst) System

A quasi-continuous burst-mode laser (QuasiModo-1000, Spectral Energies, LLC) with both diode and flashlamp Nd:YAG amplifiers was used to produce a high energy pulse train at 532 nm in a separate set of experiments. The design of the pulse-burst laser is based on master oscillator power amplifier architecture and is similar to previously reported pulse-burst lasers [26-27]. As detailed in [28], the laser is capable of producing doublets with variable inter-pulse spacing and pulse frequencies. Here, 37.5 kHz doublets separated by 3 μs were used. The pulse-burst laser generated a 10.2 ms burst every 8 seconds and the energy per pulse was 20 mJ.

Images were acquired using two high-speed CMOS cameras (Photron SA-Z). Each camera was operated at 75 kHz with a resolution of 640 × 384 pixels. The two pulses in a doublet were frame-straddled around the interframe transfer time of the cameras to produces separate images for cross-correlation analysis. In other words, the PIV repetition rate was half that of the framing-rate, or 37.5 kHz.

The two cameras were placed side-by-side as shown in Fig. 2b to extend the field of view in the streamwise direction. The resulting combined field-of-view was about 120 × 30 mm. The large size of the cameras prevented them from being placed sufficiently close to one another to image the laser sheet from a normal direction. Therefore, the cameras were angled slightly by about 3-degrees with respect to the spanwise direction so the individual imaging regions were adjacent. The cameras were also angled vertically downward by about 15-degrees to view inside the cavity directly (in this case without a mirror). Such an angle is expected to bias the vertical velocities by about 20%, though previous experience has shown that this bias does not prevent the visualization of turbulent structures [29].

The pulse-burst data were processed in a fashion similar to the 10-Hz data, except the final interrogation window size was 24 × 24 pixels. As discussed subsequently, the time-resolved vector fields were band-pass filtered around the cavity tone frequencies in order to make comparisons to the flow structure given with the 10-Hz data.

D. Unsteady Pressure Measurements

Eight dynamic pressure sensors (Kulite XCQ-062-30A or similar) having a range of about 207 kPa and a flat frequency response up until about 50 kHz were placed in the cavity fore-wall and aft-wall. The sensors were located along the span of these walls, though only data at $z = 0$ is used for analysis here. The sampling frequency was 200 kHz and the data were low-pass-filtered at 50 kHz. Previous experiments have confirmed that the cavity pressures scale with q_∞ and that the data are highly repeatable. *SPL* spectra are shown herein, which were generated using a total of at least 2 million samples and were computed using the Welch windowing algorithm in the Mathworks software package (MatLab R2013b). Blackman windows with an overlap of 50% and a window length of 10 Hz were used. Additional details on the fast-response pressure measurements system are given in [30].

III. Results and Analysis

A. Cavity Pressure Spectra

SPL spectra obtained at the fore-wall and aft-wall of the cavity are shown in Fig. 3, for the freestream Mach number of 0.91. In this case, the amplitudes of the first three Rossiter modes (M1 – M3) are quite similar and reside within a few dB of one another. A fourth cavity tone (M4) is also observed. The presence of three active modes provides a good case to test the phase-averaging and filtering algorithms developed herein to reveal the flow structure associated with a distinct cavity tone. The expected frequencies of the cavity tones can be given with the modified Rossiter relation of Heller and Bliss [10]:

$$St = \frac{f_m L}{U_\infty} = \frac{m - \alpha}{\left[M_\infty \left(1 + \frac{\gamma - 1}{2} M_\infty\right)^{-1/2} + \frac{1}{\kappa} \right]} \qquad (1)$$

where f is frequency, m is integer mode number, U_∞ is freestream velocity, γ is the ratio of specific heats, α is the phase lag, in fractions of a wavelength, which occurs in the time between the passing of a disturbance over the aft-edge of the cavity and the formation of an upstream traveling disturbance. The convective velocity of the disturbance as a fraction of U_∞ is represented by κ. Throughout the literature, the most commonly used constants for phase lag and convective velocity are 0.25 and 0.57, respectively. Using these values for α and κ in Eq. (1) gives the Rossiter-predicted frequencies listed in Table 2. The agreement with respect to the measured frequencies is within 4%.

Table 2: Measured and Predicted Cavity Tone Frequencies

M_∞	Measured f_1, f_2, f_3, f_4 (kHz)	Predicted f_1, f_2, f_3, f_4 (kHz)	Predicted λ/L (λ/D) *modes 1, 2, 3, 4*
0.91	0.69, 1.67, 2.58, 3.50	0.69, 1.61, 2.53, 3.45	1.97 (9.9), 0.85 (4.3), 0.54 (2.7), 0.39 (2.0)

Equation (1) can also be cast in terms of disturbance wavelength λ [15]:

$$\frac{\lambda}{L} = \frac{1}{m - \alpha} \left[1 + \kappa \frac{M_\infty}{\sqrt{1 + \left[(\gamma - 1)/2\right] M_\infty^{\,2}}} \right] \qquad (2)$$

Based on the predicted wavelengths listed in Table 2, the third and fourth modes are expected to contain about two and three vortices, respectively. Mode 2 should contain one vortex and a fraction of another, whereas, mode 1 will often resonate without large scale vortices. Observations confirming the expected numbers of vortices in compressible cavity flows have been reported in [15] and [16].

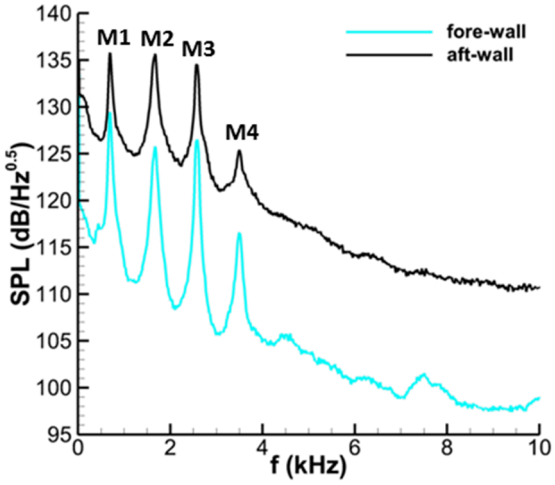

Fig. 3 Mach 0.9 sound pressure level spectra at the fore-wall and aft-wall of the cavity. M denotes a measured resonance tone.

B. Joint-Time Frequency Analysis and Conditional Averaging

Joint-time frequency analysis (JTFA) of the pressure traces was conducted using a wavelet transform. This technique shows the frequency content of the disturbances as a function of time, and has been used in other unsteady applications such as wake transition, meteorological studies, and cavity flows [15, 31-33]. The transform provides good time resolution for identifying intermittent disturbances. However, it has poor frequency resolution compared to alternate joint time-frequency methods such as the short-time-Fourier transform. The wavelet transform was computed using a Mathworks (Matlab) script provided in Ref. [33]. A Morelet mother wavelet was chosen.

An example of time-frequency content given with the wavelet analysis is given in Fig. 4a, where the wavelet transform amplitude (WT in the figure) provides a measure of the energy at a given time and frequency. The data were obtained at a sensor in the center of the fore-wall. Over the course of the 25 ms shown, the transform amplitudes of modes 1 – 3 vary substantially. Mode 1 is most active at later times, while mode 2 switches on and off throughout. Mode 3 also has short lived-bursts of high energy content. Thus, mode-switching between cavity tones 1 – 3 is clearly evident.

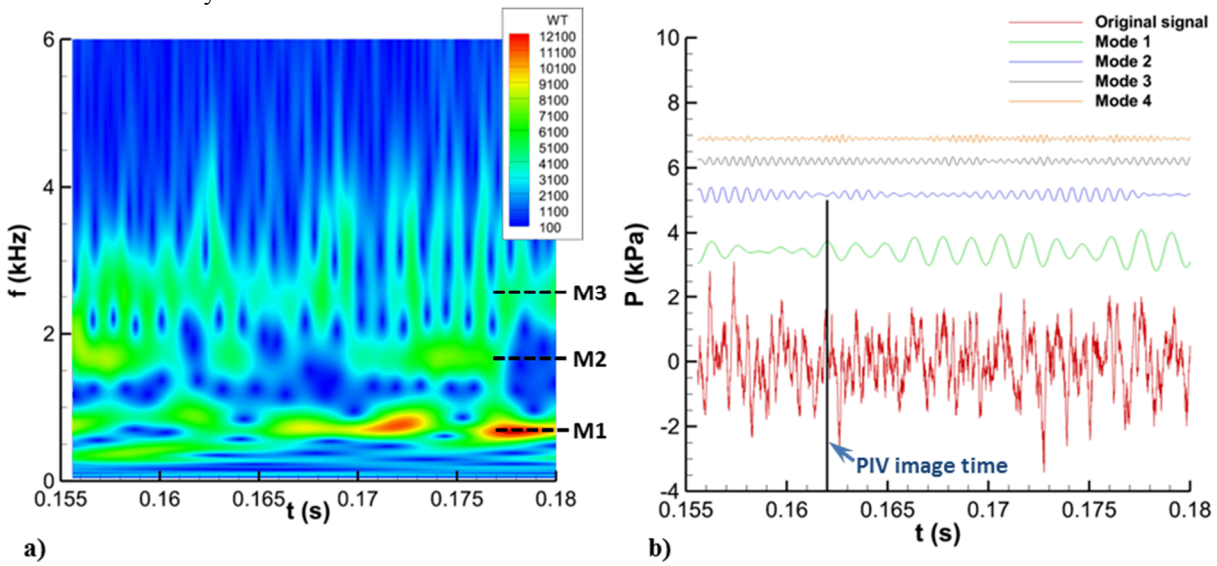

Fig. 4 Wavelet analysis: (a) joint-time frequency data during a Mach 0.9 experiment, and (b) original and bandpassed filtered pressures corresponding to cavity modes M1 – M4.

The wavelet transform was used to bandpass filter the pressure traces. This was achieved by setting wavelet transform coefficients other than those at the cavity tone frequencies to zero and then computing an inverse wavelet transform. This effectively bandpass filtered the pressure data, importantly, without a time delay. The filter frequency bandwidth was approximately 200 Hz for this process. The resulting bandpass filtered traces are shown in Fig. 4b. The bandpass filtered signals tell a story similar to that in Fig. 4a. For instance, mode 1 has the highest amplitude after 0.17 seconds and mode 2 is most active around 0.157 seconds and 0.174 seconds.

The bandpass filtered traces were used to conditionally average the stereoscopic, 10-Hz PIV images. To do so, the local maximums and minimums in each bandpass filtered trace were first found for a 14 ms trace [is that right Kat?] centered at the time of PIV image. The overall maximum and minimum peak amplitudes over this entire trace were also computed. If the amplitude of the trace was positive at the given image time, the amplitude of the nearest local maximum was then compared to the overall maximum peak amplitude. If the local maximum was greater than 50% of the overall maximum, the mode in question was considered to be active at the PIV image time. A similar threshold method was applied for the negative fluctuations in each bandpassed signal. The images passing the initial positive and negative thresholds were then binned into different phase portions of a given mode waveform.

The resulting average phases are illustrated in Fig. 5 and criteria based on slope and local amplitude for determining the phase bins are summarized in Table 3. The average phase angle associated with each condition and the corresponding number of samples is also listed in Table 3. More samples reside at the 90-degree and 270-degree conditions because the slope of the pressure waveform is lower compared to the other four phases. For all data shown herein, the conditional averaging was performed based on the bandpassed pressure signals obtained at the sensor installed in the center of the fore-wall. The fore-wall was chosen for conditioning since turbulent fluctuations are lower here in comparison to the aft-wall. Therefore, the fore-wall signal was effectively less 'noisy' than that at the aft-wall.

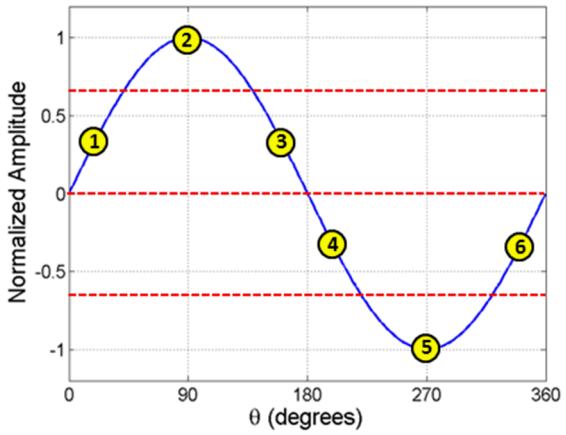

Fig. 5 Conditional averaging illustration.

Table 3: Amplitude and Slope Criteria Used for Conditional Averaging

Phase #	Amplitude Threshold	Slope Threshold	Average Phase Angle (θ)	# of Samples
1	+, 0-66% of local max	+	20	150-200
2	+, 66-100% of local max	N/A	90	300-400
3	+, 0-66% of local max	-	160	150-200
4	-, 0-66% of local min	-	200	150-200
5	-, 66-100% of local min	N/A	270	300-400
6	-, 0-66% of local min	+	340	150-200

C. Phase-Averaged 10-Hz PIV

Each PIV vector field may inherently contain flow structure and disturbance information related to several modes. Or, a given mode may be substantially more active than the other modes at a given time. In either case, it is difficult to ascertain the flow structure associated with a given cavity tone in the 10-Hz PIV. An example of this is given in Fig. 6, which plots the instantaneous streamwise contours and streamtraces corresponding to the time of 0.162 seconds in Fig. 4. Three vortical disturbances are apparent in the flow (labels A, B, and C). At this time in

the pressure data, modes 1, 3, and 4 are near a peak, while mode 2 is mostly inactive. Determining the flow structure associated with the pressure data without further analysis, such as conditional averaging, is difficult.

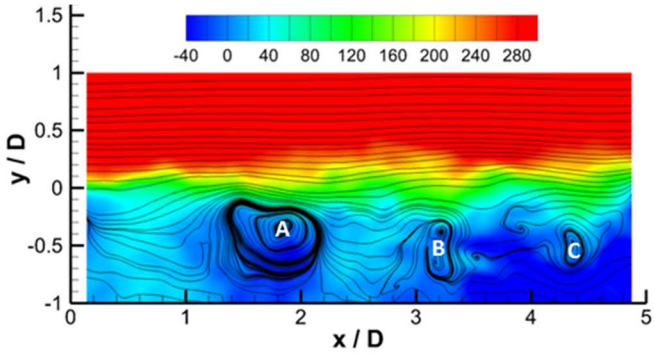

Fig. 6 Mach 0.91 instantaneous streamwise velocity contours and streamtraces corresponding to the time 0.162 seconds in the pressure data of Fig. 4.

Conditionally averaged velocity contours corresponding to cavity mode 1 are shown in Fig. 7. The velocities are plotted as the difference between the streamwise phase-averaged velocity U_θ and the mean streamwise velocity U. As discussed in Hussain [34], the result of such a subtraction is expected to reveal the coherent structures in a turbulent flow. The wavelength of mode 1 is expected to be about $2L$ (Table 2) making it difficult to identify the convection of structures using only six phases. For this reason, only the most informative phases containing the greatest number of samples (θ = 90-degrees and θ = 270-degrees) are shown here. At 90-degrees the velocity is decreased in the entire streamwise extent of the shear layer. In contrast, when the phase is shifted by 180-degrees, an increase in shear layer streamwise velocity is clearly observed. These results suggest mode 1 to be associated large scale changes in the shear layer. Moreover, the figure suggests mode 1 is also associated with large scale velocity variations in the aft-end of the cavity near the recirculation region. The streamtraces in the figure seem to suggest that the recirculation region does not exhibit much translation, however.

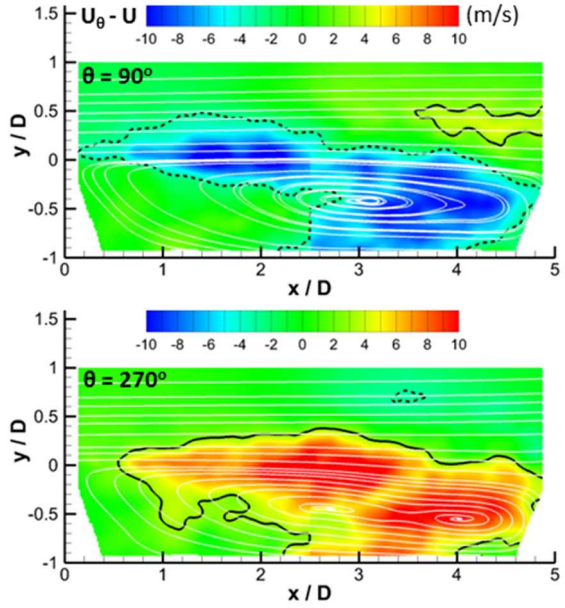

Fig. 7 *Mode 1 coherent structures* corresponding to a pressure peak (θ = 90-degrees) and pressure trough (θ = 270-degrees) in the bandpassed pressure data. Streamtraces corresponding to the phase averaged velocity are shown as white lines. The black lines correspond to contour values of 4 m/s (solid) and -4 m/s (dashed) to highlight structure.

Coherent structures corresponding to mode 2 are displayed in Fig. 8. The left side of the figure shows the difference between the wall-normal phase-averaged velocity and the mean wall-normal velocity ($V_\theta - V$). The right

side of the figure shows $U_\theta - U_\infty$. The vertical velocities associated with mode 2 reveal a clear convection of organized structure as the phase angle increases from 20-degrees to 340-degrees. At 20-degrees, a region of organized positive vertical velocity appears near the leading-edge of the cavity (label A). With continuing time (increasing phase angle), this structure advects downstream reaching a position near $x/D = 3.5$ at 340-degrees. Upon completion of a full 360-degree cycle it is apparent that the upstream region of positive vertical velocity (A) moves downstream to become the larger region of positive vertical velocity (A'). Similar observations are seen in the regions of negative vertical velocities (B and B'). The streamwise coherent velocities exhibit a more complex flow structure. Nevertheless, a similar convection of negative (C and C') and positive velocities (D) can be observed.

Similar observations are made in the coherent velocities associated with mode 3 (Fig. 9). An obvious convection in vertical flow structure is seen with increasing phase angle. Once again, the structure of the streamwise coherent velocities is more complicated, though alternating positive and negative regions are still apparent. As the coherent structures propagate downstream they rise upward as illustrated with the dashed violet lines in the figures at $\theta = 270$-degrees. Inspection of the mode 2 coherent structures also shows an increasing vertical displacement as the structures move downstream.

As the mode number increases from 1 – 3 the wavelengths of the coherent velocity fields decrease, as expected. Under the classical interpretation, the disturbances in Rossiter modes should be associated with convecting regions of spanwise vorticity. With this interpretation in mind, vortices are sketched in Fig. 8 and Fig. 9 according to the vertical coherent velocity fields. To further quantify vortex spacing, the coherent vertical velocity across the length of the cavity is plotted for mode 2 in Fig. 10a and for mode 3 in Fig. 10b. Plots are shown at phase angles of 90-degrees and 270-degrees since they contained the highest number of samples and therefore exhibited the greatest statistical convergence. When only these two phases are plotted, the profiles give the appearance of a standing wave. The mode 2 profiles cross zero at similar streamwise stations giving the appearance of nodes at $x/D = 1.8$, and $x/D = 3.7$. Similar nodes appear in the mode 3 subfigure at $x/D = 1.3$, 3.8, and 4.7. An additional node likely exists around $x/D = 2.7$, but is masked by a lack of convergence of the 90-degree data (e.g., see the corresponding contour plot in Fig. 9).

Vortex spacing can be estimated from Fig. 10 using several different locations along the waveforms. For example, in Fig. 10a, the trough-to-trough distance in the 270-degrees plot and the peak-to-peak distance in the 90-degrees profile suggest a wavelength of about $3D - 3.5D$. Similar values are reached if the wavelength is taken to be double the peak-to-trough distance along a given waveform. A higher value of about $4D$ can be found if the wavelength is taken to be double the distance from node-to-node. In any event, comparison of these values to those in Table 2 suggests that the average measured vortex spacing is lower than that expected from the Rossiter relation. Using a similar methodology for Fig. 10b suggests the wavelength in the upstream-half of the cavity is about $2D$, while the spacing in the downstream-half of the cavity is about $2.3D$. Thus, the spacing increases as the disturbances propagate downstream. The latter wavelength is approaching the Rossiter prediction of $2.7D$, but on average the vortex spacing appears to be lower than expected. Such an observation would be consistent with a lower convective velocity than the commonly used $0.57U_\infty$, a value which also gives good agreement with the measured cavity tone frequencies here (Table 2). In a numerical study with $L/D = 5$ and $M_\infty = 0.85$, Larchevêque et al. [16] reported an average convective velocity of $0.52U_\infty$ based on two-point correlations of vertical velocity. Here, if wavelengths of $3.5D$ and $2.2D$ are used for modes 2 and 3, respectively, the convective velocity computes to be even lower at about $0.47U_\infty$. Such a difference warrants further investigation and a quantification of convective velocity with a finer spatial resolution along the cavity length.

D. Bandpass Filtered Pulse-Burst PIV

The pulse-burst PIV data provide an alternative opportunity to resolve the flow structure associated with a given cavity tone. Like the 10 Hz data, each instantaneous vector field may contain flow structures associated with several cavity modes. To resolve the flowfield information of the cavity tones, the velocity fields were bandpass filtered in the time domain about each of the cavity tone frequencies. In each case, the width of the filter was approximately 100 Hz and it exhibited a sharp roll-off. [Srini, please add a little more information on your time-domain filter]

Bandpassed filtered velocities corresponding to the third cavity tone are displayed in Fig. 11. Instantaneous contours of filtered vertical velocity (v_{f3}) are shown for an entire period of a mode 3 oscillation. The sequence was chosen at random without knowledge of the cavity pressures. The time between each velocity field is 53.3 μs (i.e., the figure is displayed at 18.75 kHz, or half the sampling rate of the PIV data). Though a full exploration of the pulse-burst data is well beyond the scope of this paper, some comparisons to the 10-Hz conditionally averaged results are helpful here to validate the phase-averaging methodology. As time progresses in the figure, convection

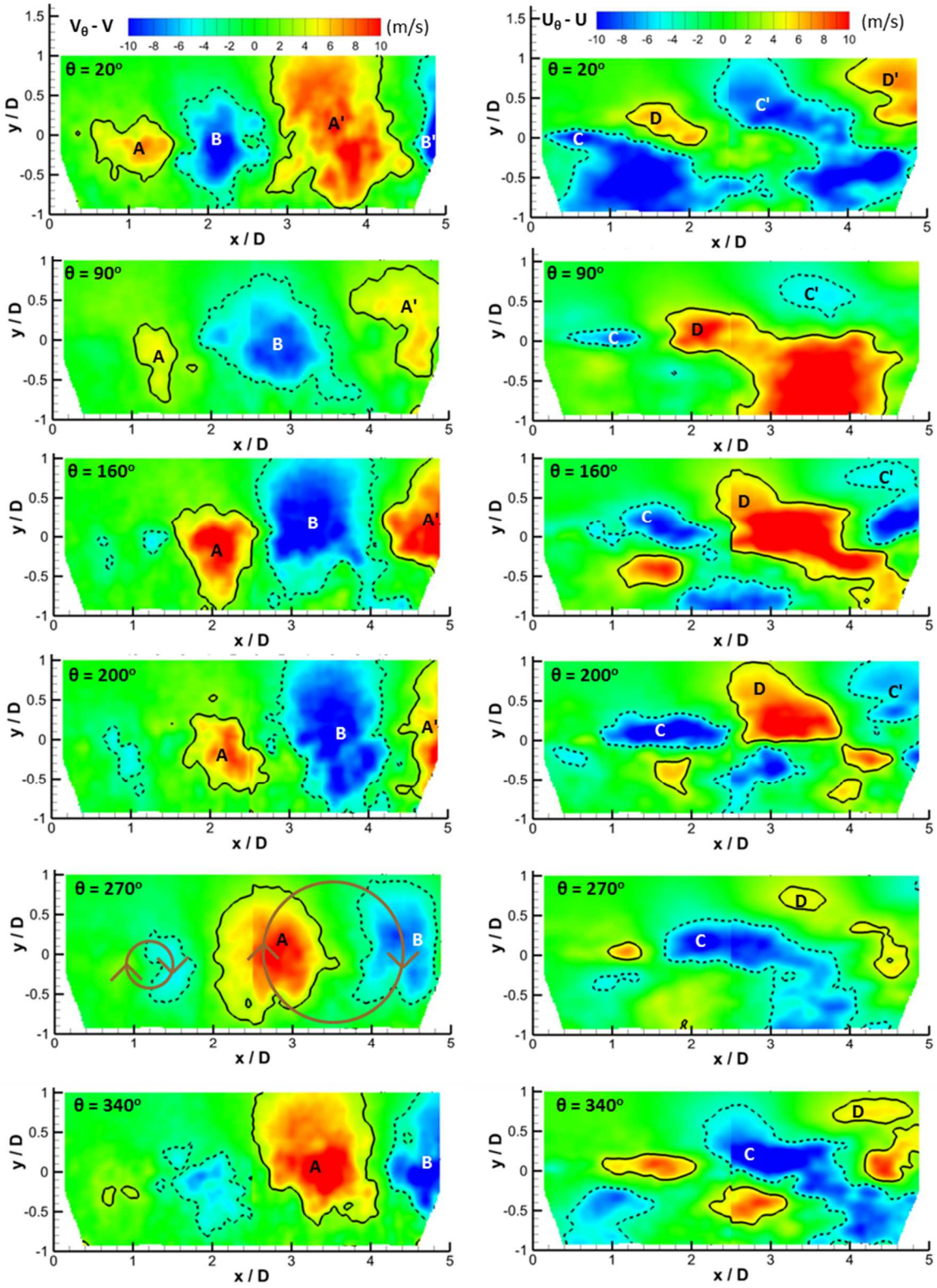

Fig. 8 *Mode 2 coherent structures* corresponding to phase angles θ of 20, 90, 160, 200, 270, and 340 degrees in the bandpassed pressure data. The left side of the figure shows $V_\theta - V$ with solid lines at contour values of 3 m/s and dashed lines at -3 m/s. The right side of the figure shows $U_\theta - U$ with contour lines at 4 m/s and -4 m/s.

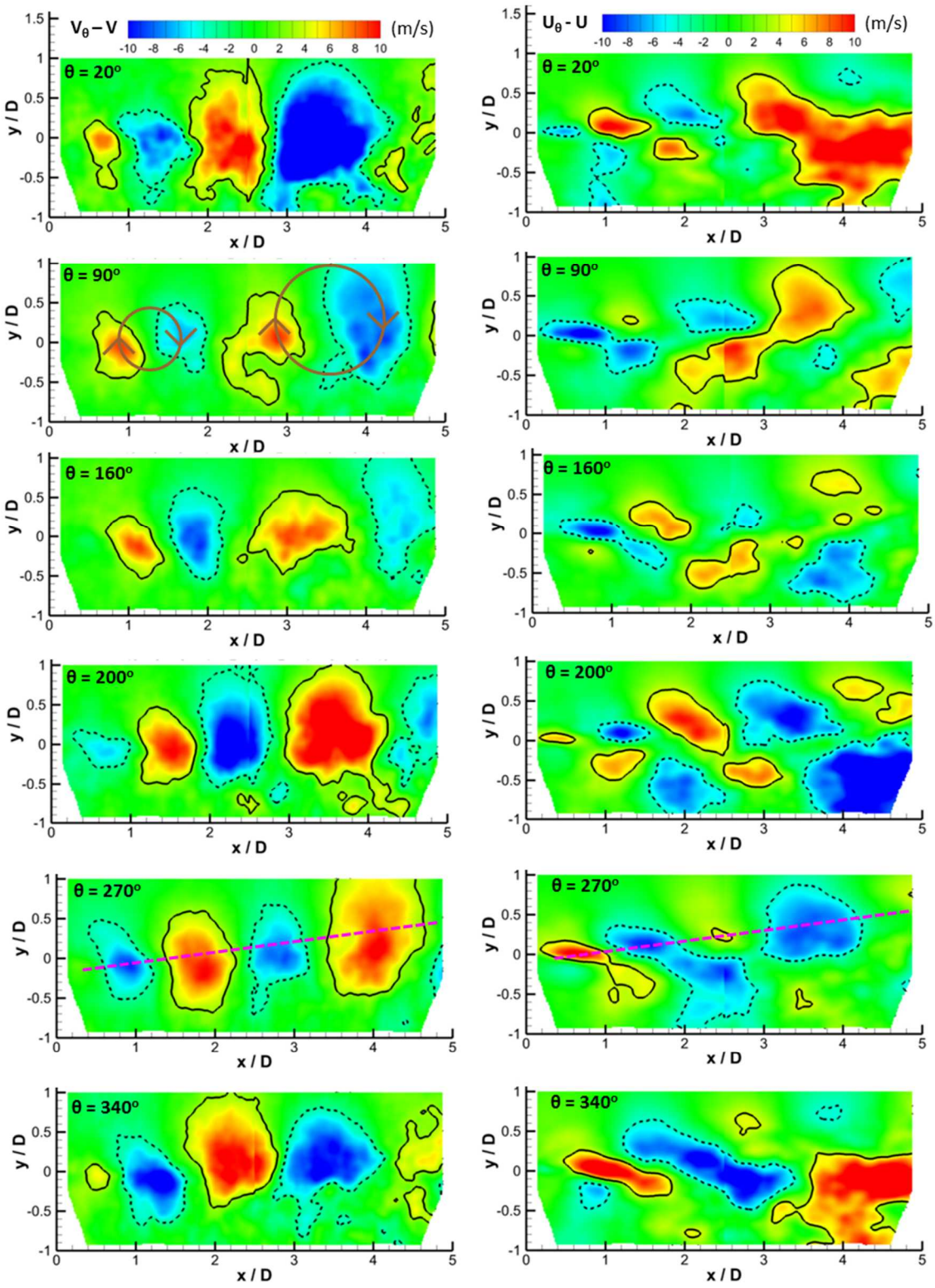

Fig. 9 *Mode 3coherent structures* corresponding to phase angles θ of 20, 90, 160, 200, 270, and 340 degrees in the bandpassed pressure data. The left side of the figure shows $V_\theta - V$ with solid lines at contour values of 3 m/s and dashed lines at -3 m/s. The right side of the figure shows $U_\theta - U$ with contour lines at 4 m/s and -4 m/s.

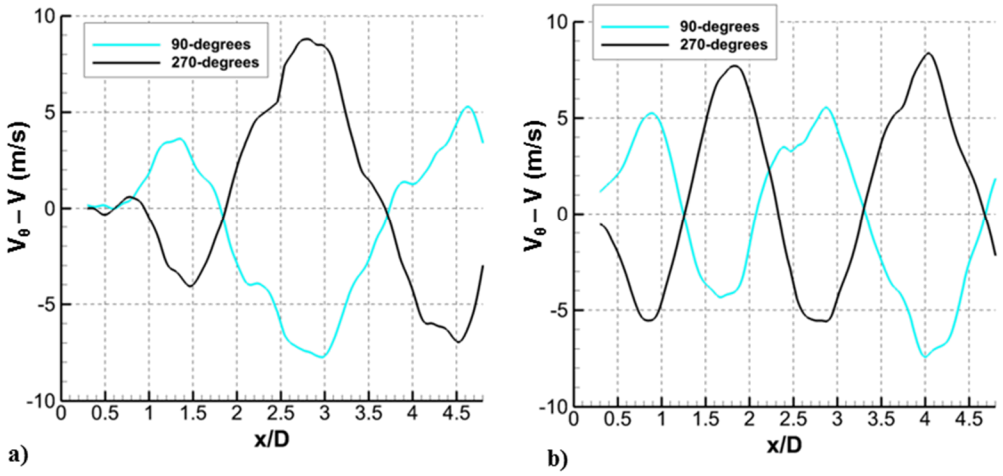

Fig. 10 Coherent vertical velocities across the cavity length averaged over the shear layer (-0.4 < y/*D* < 0.4): (a) mode 2, and (b) mode 3.

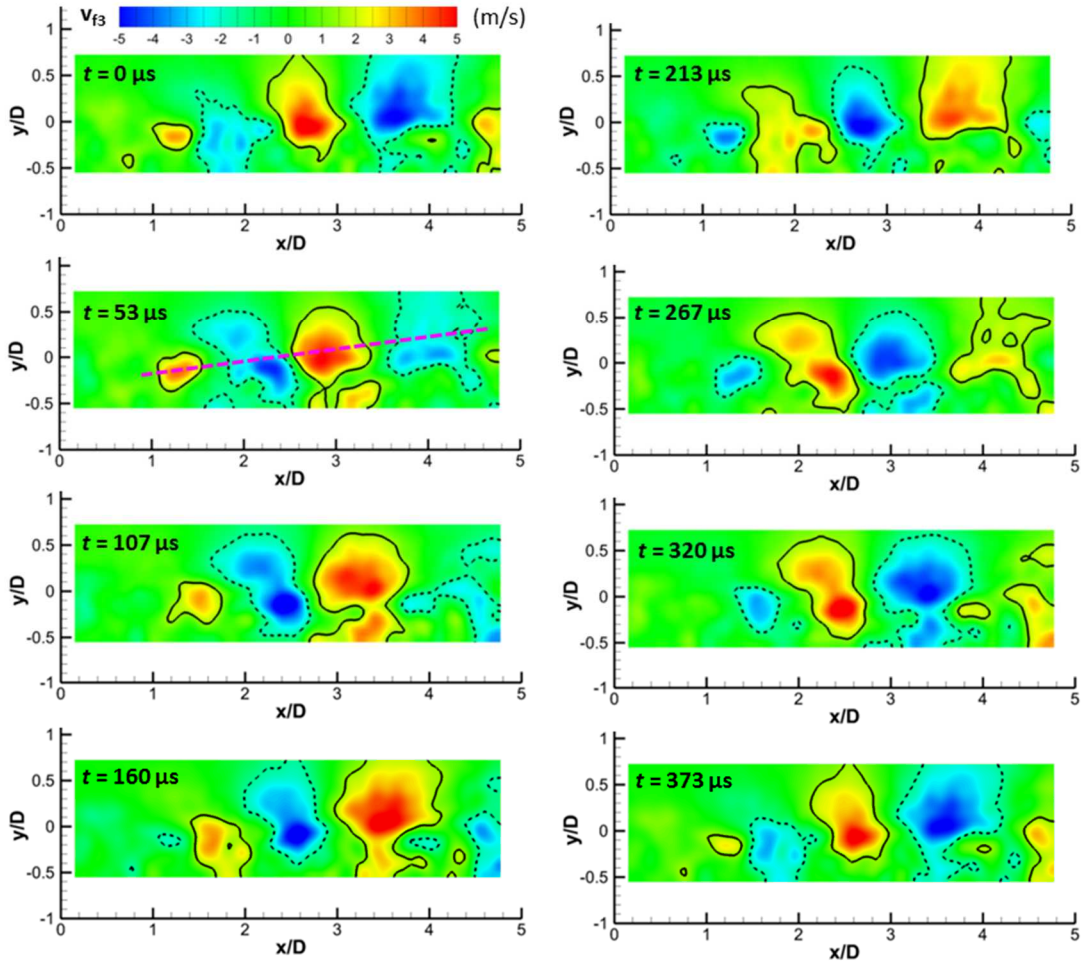

Fig. 11 *Mode 3 time-resolved instantaneous contours of vertical velocity* (v_{f3}) obtained from bandpass filtering the pulse-burst data over a random time interval. The black contour lines are at 1.5 m/s (solid) and -1.5 m/s (dashed).

of vertical flow structure is observed. The fluctuation levels in the filtered pulse-burst data are about half of that in the10-Hz data shown in Fig. 11, perhaps because the pulse-burst data were not conditioned on strong mode 3 events as in the phase-averaged data. Nevertheless, there are qualitative similarities between the results given by the two methods. Like in Fig. 9, the time-resolved structures grow in size with downstream convection, while also rising vertically (t = 53 μs). As the structures reach the aft-wall, they become less organized and lose coherence, an observation consistent with cavity pressure measurements [30, 35-36]. The spacing between regions of organized vertical velocities is also similar to that in the phase-averaged results. Inspection of Fig. 11 suggests the disturbance wavelength to be near *2D*. Finally, though not shown here, the filtered vertical velocities fields associated with mode 2 were also observed to be qualitatively similar to the conditionally average data. Further analysis and discussion of the pulse-burst data will be presented in future papers.

E. Proper Orthogonal Decomposition (POD)

As a third method to elucidate flow structure, POD analysis [37, 38] was performed on the stereoscopic dataset using the LaVision software package DaVis v8.2. In short, the method used the 3000 vector fields as inputs to form an eigenvalue problem. Optimal basis functions to characterize the flowfield were then found by solving the eigenvalue problem. The eigenfields resulting from this process give the POD modes. By definition, POD analysis with 3000 inputs will yield 3000 outputs or POD modes. The percentage of energy in the first 30 modes for the current POD is shown in Fig. 12. According to this analysis, the first mode has about 10% of the total energy and the energy fraction decreases to about 2% by the sixth mode.

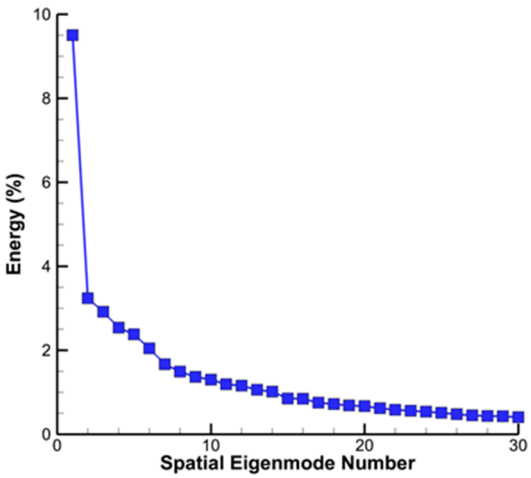

Fig. 12 Fraction of total energy in first 30 POD modes.

POD results are shown in Fig. 13, where contributions from each velocity component are given for the six most energetic modes. Some qualitative inferences can be drawn from the figure. The first POD mode is associated with large scale streamwise and wall-normal energies throughout most of the shear layer. Based on the conditional averaging of the very same dataset shown in Fig. 7, it seems likely that the first POD mode here is associated with the first Rossiter mode. Murray et al. [16] were able to reach a similar conclusion with POD analysis, without comparison to phase-averaged velocity fields. The vertical component of POD mode 2 seems somewhat similar to the coherent vertical velocity fields shown for cavity mode 2 in Fig. 8. The large positive (red) and negative (blue) wall-normal structures in the POD resemble the large vortices seen near the aft-end of the cavity during this mode. Moreover, the smaller positive and negative regions in the POD may be associated with the smaller coherent structures observed near the upstream end of the cavity in Fig. 8. In contrast, the corresponding streamwise contour plot for POD mode 2 does not seem very similar to the coherent streamwise structures shown in Fig. 8. The spatial frequency of the POD mode appears to be lower than the cavity mode. The third POD mode exhibits less similarity to the cavity modes. For instance, the streamwise energy of the third mode does not resemble the coherent streamwise velocities in the phase-averaged data. Rather, the mode gives the impression it may be associated with rotation in the recirculation region. The vertical portion of POD mode 3 may have some relation to cavity mode 2, although it is difficult to say with any certainty.

POD modes 4 – 6 continue to show some qualitative similarities to cavity tones, although an obvious pattern is lacking. The wall-normal component of the fourth POD mode has a spatial distribution similar to that seen in cavity mode 3 (Fig. 9). The corresponding streamwise distribution of the fourth POD mode, however, looks more akin to the coherent streamwise velocities of cavity mode 2. The fifth POD mode is dominated by spanwise energy and has a distribution somewhat similar in appearance to the streamwise contours of the third POD mode. Finally, the sixth POD mode has a streamwise distribution with some similarities to cavity tones 2 and 3. The vertical content of the sixth mode resembles the vertical coherent velocity fields of cavity tone 3, though the sixth mode may also be influenced by a higher-order cavity mode, such as tone four.

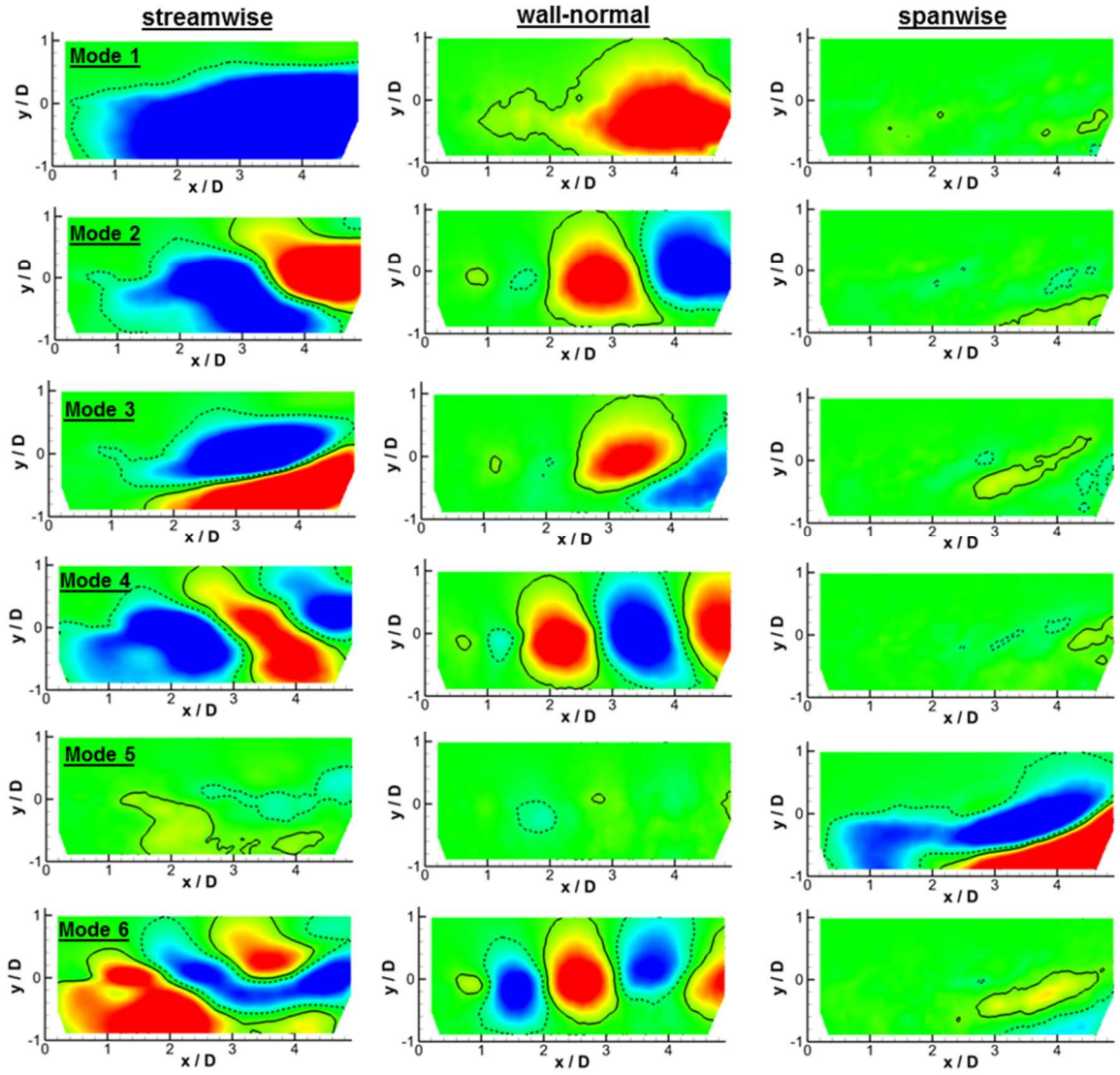

Fig. 13 Six most energetic POD modes decomposed into streamwise (left), wall-normal (middle), and spanwise (right) components. The contour band is symmetric and has the same scaling in each subfigure.

Although POD can provide insight into the dominant dynamics of a turbulent flow, the results in cavity flows can be ambiguous since the method does not provide any frequency information associated with the modes. Here some qualitative similarities are observed in comparison to the phase-averaged data. Without the corresponding conditionally averaged data, however, interpretation of the POD results would prove more difficult.

IV. Conclusions

Particle image velocimetry (PIV) measurements along with simultaneous fast-response pressures were used to identify the flow structure occurring associated with cavity resonant tones. Experiments were performed at Mach 0.91in a cavity having a length-to-depth ratio of five and a square planform. The incoming boundary layer was turbulent with a 99% boundary layer thickness equal to about half the cavity depth.

Two independent PIV datasets were utilized. The first was stereoscopic PIV obtained at a repetition-rate of 10-Hz. Additionally, two-component time-resolved data were acquired using a pulse-burst laser. The primary analysis performed in the current work was on the stereoscopic data, whereas the time-resolved data were used mostly to validate the observations made with the 10-Hz data.

The first three cavity modes were active with relatively equal amplitudes and their frequencies were well predicted by the Rossiter relation. Joint-time frequency analysis (JTFA) on the pressure data revealed instances of mode-switching and cases where modes existed simultaneously. To separate the effects from the various cavity tones, the pressure data were bandpass filtered about the cavity tone frequencies using the wavelet transform coefficients of the JTFA analysis. The stereoscopic, 10-Hz PIV data were then phase-averaged according to the bandpassed pressures. The coherent velocity fields were used to reveal the flow structure associated with the most active cavity resonant tones.

The phase-averaged results showed the first Rossiter mode to be associated with large scale streamwise velocity fluctuations in the shear layer. The second and third modes contained organized structures consistent with the classical Rossiter interpretation of convecting vortical disturbances. The spatial wavelengths of the cavity tones were estimated based on the vertical coherent velocity fields. Despite an excellent agreement between the Rossiter-predicted frequencies and the frequencies measured with the pressure sensors, the spatial wavelengths were found to be less than those predicted by the Rossiter relation. To validate the phase-averaged method, the time-resolved PIV data were bandpass filtered about the cavity tone frequencies to reveal flow structure. The resulting spacing between disturbances in the filtered, time-resolved data was similar to that found in the phase-averaged flowfields.

Proper orthogonal decomposition (POD) was performed on the stereoscopic data as a third way to elucidate coherent structures. The results revealed POD modes with qualitatively similar flow structure as the phase-averaged. However, a pattern in the POD mode number with respect to cavity mode number was unclear.

Future work will use the pulse-burst PIV data to further investigate and characterize the flow structure associated with transonic cavity resonance.

Acknowledgments

The authors would like to acknowledge Dr. Edward DeMauro and Dr. Matthew Barone for very valuable discussions on coherent structures in turbulence and on cavity flows. Wavelet software was provided by C. Torrence and G. Compo, and is available at URL: http://paos.colorado.edu/research/wavelets/.

References

[1] Rossiter, J. E., "Wind-Tunnel Experiments on the Flow Over Rectangular Cavities at Subsonic and Transonic Speeds," Aeronautical Research Council Reports and Memoranda, October 1964.

[2] Tracy, M. B., and Plentovich, E. B., "Cavity Unsteady-Pressure Measurements at Subsonic and Transonic Speeds," NASA Technical Paper 3669, December 1997.

[3] Dix, R. E., and Bauer, R. C., "Experimental and Predicted Acoustic Amplitudes in a Rectangular Cavity," AIAA Paper 2000-0472.

[4] Rockwell, D., and Naudascher, E., "Review-Self Sustaining Oscillations of Flow Past Cavities," *Journal of Fluids Engineering*, Vol. 100, 1978, pp. 152-165.

[5] Rowley, C. W., and Williams, D. R., "Dynamics and Control of High-Reynolds-Number Flow over Open Cavities," *Annual Review of Fluid Mechanics*, Vol. 38, 2006, pp. 251-276.

[6] Cattafesta, L. N., Song, Q., Williams D. R., Rowley C. W., and Alvi, F. S., "Active control of flow-induced cavity oscillations," *Progress in Aerospace Sciences*, Vol. 44, 2008, pp. 479-502.

[7] Rockwell, D., and Naudascher, E., "Self-sustained oscillations of impinging free shear layers," *Annual Review of Fluid Mechanics*, Vol. 11, 1979, pp. 67-94.

[8] Rowley, C. W., Williams, D. R., Colonius, T., Murray, R. M., MacMartin, D. G., and Fabris, D., "Model-based control of cavity oscillations, part II: System identification and analysis," AIAA Paper 2002-0972.

[9] Rowley, C. W., Williams, D. R., Colonius, T., Murray, R. M., & Macmynowski, D. G., "Linear models for control of cavity flow oscillations," *Journal of Fluid Mechanics*, Vol. 547, 2006, pp. 317-330.

[10] Heller, H. H., and Bliss, D. B., "The Physical Mechanism of Flow Induced Pressure Fluctuations in Cavities and Concepts for Suppression," AIAA Paper 75-491.

[11] Ukeiley, L. S., and Murray, N. E., "Velocity and Surface Pressure Measurements in an Open Cavity," *Experiments in Fluids*, Vol. 38, 2005, pp. 656–671.
[12] Krishnamurty K., "Acoustic radiation from two-dimensional rectangular cutouts in aerodynamic surfaces," NACA TN 3487, 1955.
[13] Sarohia, V., "Experimental investigation of oscillations in flows over shallow cavities," *AIAA Journal*, Vol. 15, No. 7, 1977, pp. 984-990.
[14] Kegerise, M. A., "An Experimental Investigation of Flow Induced Cavity Oscillations," Ph.D. Thesis, Department of Mechanical Engineering, Syracuse University, New York, USA, 1999.
[15] Kegerise, M. A., Spina, E. F., Garg, S., Cattafesta, L. N., "Mode-Switching and Nonlinear Effects in Compressible Flow Over a Cavity," *Physics of Fluids*, Vol. 16, No. 3, 2005, pp. 678-687.
[16] Larchevêque, L., Sagaut, P., Lê, T. P., and Compte, P., "Large-eddy simulation of a compressible flow in a three-dimensional open cavity at high Reynolds number," *Journal of Fluid Mechanics*, Vol. 516, 2004, pp. 265-301.
[17] Murray, N. E., and Ukeiley, L. S., "Modified quadratic stochastic estimation of resonating subsonic cavity flow," *Journal of Turbulence*, Vol. 8, No. 53, 2007, pp. 1-22.
[18] Brès, G. A., and Colonius, T., "Three-Dimensional Instabilities in Compressible Flow over Open Cavities," *Journal of Fluid Mechanics*, Vol. 599, 2008, pp. 309-339.
[19] Song, Q., Closed-Loop Control of Flow-Induced Cavity Oscillations, Ph.D. Thesis, Department of Mechanical and Aerospace Engineering, University of Florida, Gainesville, USA, 2008.
[20] Murray, N. E., Sallstrom, E., and Ukeiley, L., "Properties of Subsonic Open Cavity Flow Fields," *Physics of Fluids*, Vol. 21, No. 9, 2009.
[21] Wagner, J. L., Casper, K. M., Beresh, S. J., Pruett, B. O., Spillers R. W., and Henfling, J. F., "Mitigation of Wind Tunnel Wall Interactions in Subsonic Cavity Flows," *Experiments in Fluids* (published online), DOI: 10.1007/s00348-015-1924-8, 2015.
[22] Samimy, M., and Lele, S. K., "Motion of Particles with Inertia in a Compressible Free Shear Layer," Physics of Fluids A, Vol. 3, No. 8, 1991, pp. 1915-1923.
[23] Beresh, S. J., Wagner, J. L., Pruett, B. O., Henfling, J. F., and Spillers, R. W., "Supersonic Flow over a Finite-Width Rectangular Cavity," *AIAA Journal*, Vol. 53, No. 2, 2014, pp. 296-310.
[24] Walker, S., "Two-Axes Scheimpflug Focusing for Particle Image Velocimetry," Measurement Science and Technology, Vol. 13, No. 1, 2002, pp. 1-12.
[25] Beresh, S. J., Wagner, J. L., Henfling, J. F., Spillers, R. W. and Pruett, B. O., "Width Effects in Transonic Flow of a Rectangular Cavity," *AIAA Journal* (accepted for publication), 2015.
[26] Slipchenko, M. N., Miller, J. D., Roy, S., Gord, J. R., Danczyk, S. A., and Meyer, T. R., "Quasi-Continuous Burst-Mode Laser for High-Speed Planar Imaging," *Optics Letters*, Vol. 37, No. 8, pp. 1346-1348, 2012.
[27] Slipchenko, M. N., Miller, J. D., Roy, S., Gord, J. R., and Meyer, T. R., "All-Diode-Pumped Quasi-Continuous Burst-Mode Laser for Extended High-Speed Planar Imaging," *Optics Express*, Vol. 21, No. 1, pp. 681-689, 2013.
[28] Beresh, S. J., Kearney, S. P., Wagner, J. L., Guildenbecher, D. R., Henfling, J. F., Spillers, R. W., Pruett, B. O., Jiang, N., Slipchenko, M., Mance, J., and Roy, S., "Pulse-Burst PIV in a High-Speed Wind Tunnel," AIAA Paper 2015-1218.
[29] Beresh, S. J., Wagner, J. L., and Pruett, B. O. M., "Particle Image Velocimetry of a Three-Dimensional Supersonic Cavity Flow," AIAA Paper 2012-0030.
[30] Wagner, J. L., Casper, K. M., Beresh, S. J., Hunter, P. S., Spillers, R. W., Henfling, J. F., Mayes, R. L., "Fluid-Structure Interactions in Compressible Cavity Flows," *Physics of Fluids* (accepted for publication), 2015.
[31] Shaikh, F. N. and Gaster, M., "The Non-Linear Evolution of Modulated Waves in a Boundary Layer," Journal of Engineering Mathematics, Vol. 28, 1994, pp. 55–71.
[32] Jordan, D., Miksad, R. W., and Powers, E. J., "Implementation of the Continuous Wavelet Transform for Digital Time Series Analysis," Review of Scientific Instruments, Vol. 68, No. 3, March 1997, pp. 1484–1494.
[33] Torrence, C. and Compo, G. P., "A Practical Guide to Wavelet Analysis," Bulletin of the American Meteorological Society, Vol. 79, No. 1, 1998, pp. 61–78.
[34] Hussain, A. K. M., "Coherent Structures and Turbulence," *Journal of Fluid Mechanics*, vol. 173, pp. 303-356, 1986.
[35] Zhuang, N., Alvi, F. S., Alkislar, M. B., and Shih, C., "Supersonic Cavity Flows and Their Control," *AIAA Journal*, Vol. 44, No. 9, 2006, pp. 2118-2128.
[36] Casper, K. M., Wagner, J. L., Beresh, S. J., Henfling, J. F., Spillers, R. W., and Pruett, B. O., " Complex geometry effects on subsonic cavity flows," AIAA Paper 2015-1291.
[37] Holmes, P., Lumley, J., and Berkooz, G., *Turbulence, Coherent Structures, Dynamical Systems and Symmetry*, Cambridge University Press, Cambridge, 1996.
[38] Sirovich, L., "Turbulence and the dynamics of coherent structures. Part I: Coherent structures." *Quarterly of applied mathematics*, Vol. 45, 1987, pp. 561 – 571.